PROCEEDINGS OF SPIE

Optical effects of a temperature-mismatched supersonic mixing layer

Aaron Fassler, Sergey Leonov, Stanislav Gordeyev

SPIE.

Optical Effects of a Temperature-Mismatched Supersonic Mixing Layer

Aaron Fassler[a], Sergey Leonov[a], and Stanislav Gordeyev[a]

[a]University of Notre Dame, Notre Dame, IN, United States

1. ABSTRACT

The aero-optical distortions caused by supersonic mixing layers over an optical window are relevant to the performance of hypersonic vehicles. Such mixing layers are typically temperature-mismatched due to a need to cool the optical window. To investigate the effect of the mismatched temperature across the mixing layer created by blowing a cool air over a flat window, optical measurements of an $M = 2$ freestream flow with an $M \approx 0.56$ cooling two-dimensional jet were taken using Shack-Hartmann WFS and Schlieren photography techniques. Total temperature of the freestream flow was varied from $295K$ to $750K$, while the total temperature of the cooling jet was kept constant at $295K$. Parameters of the mixing flow were examined using optical velocity methods. A new scaling method for aero-optical distortions in a temperature-mismatched, species matched supersonic mixing layer is proposed, providing an improved linear fit compared to the previous model.

2. INTRODUCTION

Hypersonic vehicles are becoming essential to the security of the United States and its partner nations. Critical missions include reconnaissance vehicles for gathering information anywhere in the world at short notice; high-speed, maneuverable missile-defense interceptors; hyper-velocity projectiles; and Conventional Prompt Strike weapons. Hypersonic flows around these vehicles are characterized by high stagnation temperatures, strong shock waves, and boundary layers with large temperature and density gradients. Many engineering and scientific challenges, such as reducing drag, mitigating thermal loads, advances in ramjet and scramjets, etc., have to be overcome for reliable hypersonic vehicles to become a reality. Of equal importance, hypersonic reconnaissance vehicles and interceptors require integrated optical sensors. Understanding the effects of both supersonic and hypersonic flows on the optical sensor performance, the so-called aero-optical effects, is a crucial requirement for such systems.

To successfully track a target, hypersonic vehicles typically use IR imaging cameras, usually behind a flat window mounted near the front of the vehicle, as shown in Fig. 1(a). The vehicle may also have side windows to send and receive data via laser beams as part of a high-speed and secure communication system. Since hypersonic flows significantly heat the vehicle surface, these windows need proper thermal protection. This is often achieved by blowing a coolant gas, such as nitrogen or helium, over the window to displace the hot air away from it.[1-4] While this approach does provide the needed window cooling, the mismatch in the velocity and density along the interface between the coolant gas and the ambient air forms a mixing shear layer over the window which introduces extra wavefront disturbances, as shown in Fig. 1(a).

When an optical signal travels through a hypersonic flow field, a detailed understanding of the flow field properties is essential to accurately determine the optical distortions and ultimate sensor performance. The hypersonic flow field is very complex, which includes nonequilibrium, reactive flows (i.e., chemistry), energy transfer between molecular energy modes, turbulence, boundary layers, unsteadiness, and instabilities, all of which can affect and degrade optical signals either directly or indirectly.

Density variations due to vortical structures formed inside the mixing layer and the bow shock result in significant aero-optical distortions on an outgoing laser beam or incoming light. The aero-optical distortions, denoted as the Optical Path Difference (OPD), are proportional to the integral of the fluctuating density field,

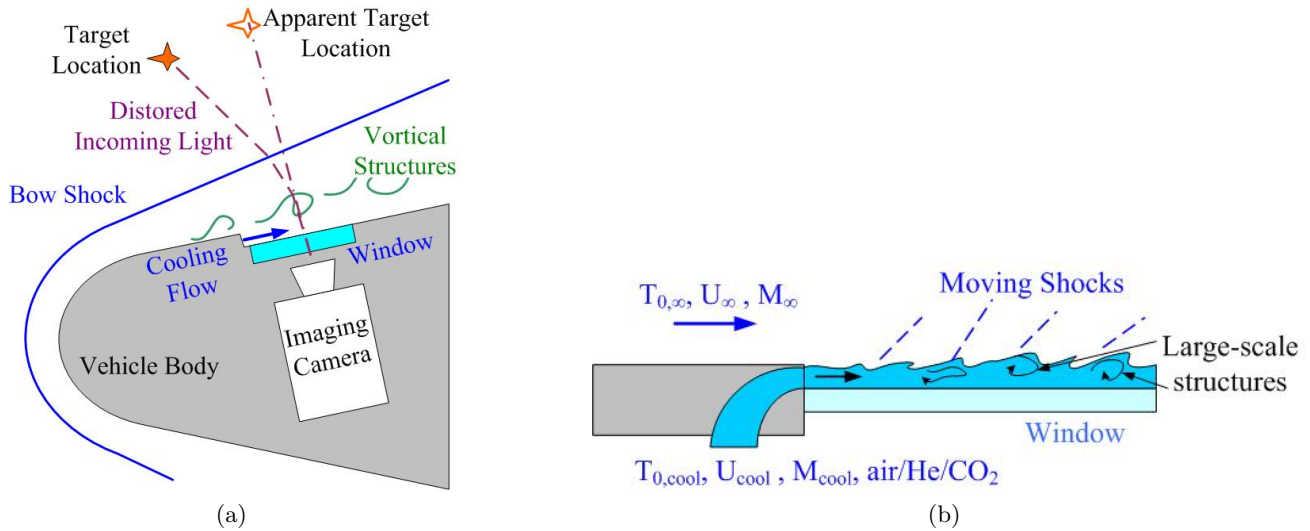$$OPD(x,z,t) = K_{GD} \int \rho'(x,y,z,t)dy \ , \tag{1}$$

Figure 1: (a) Aero-optical environment around a seeker window with a cooling flow in hypersonic flow, and associated image distortion. (b) Parameters of the mixing layer.

where K_{GD} is the Gladstone-Dale constant, and the integration is performed in the beam propagation direction.[5] Typically, the level of the aero-optical distortions is quantified by the time-averaged spatial root-mean-square of the OPD-field,

$$OPD_{rms} = \overline{\langle [OPD(x,z,t)]^2 \rangle_{x,z}} , \tag{2}$$

where the angular brackets denote spatial averaging over the beam aperture and the overbar denotes time-averaging. The destructive interference of the distorted laser beam at the target results in a significant reduction of the laser intensity on a distant target,[5,6] and unsteady aero-optical distortions deteriorate visual representations of the target.[4,6,7] In addition, unsteady aero-optical distortions will result in an overall change in direction of the incoming or outgoing beam, called a boresight error (BSE), as shown in Fig. 1(a).

In real-world applications, a cooler gas is blown over the window to displace and prevent the hotter freestream gas from reaching the window, thus keeping the window temperature within a pre-determined range. The amount of cooling depends on the velocity, U_{cool}, static pressure, P_{cool}, and stagnation temperature, $T_{0,cool}$, of the coolant gas, as well as the gas type, listed in Figure 1(b). On the one hand, high velocities, pressures, and cooler temperatures do certainly provide better cooling. On the other hand, the mismatch in velocity between the cooling gas and the freestream will enforce the inviscid inflection instability mechanism, resulting in the formation of large-scale shear-layer structures. Enhanced entrainment of hot freestream gas into the cooler region near the window will reduce the efficiency of the window cooling and, more importantly, create additional density gradients, and associated aero-optical distortions. A mismatch of the static pressure of the two streams will result in either an over- or an under-expanded cooling jet. Deformations of the interface between the cooling jet and the freestream, such as those resulting from shear-layer structures due to inflection point instability, will lead to the formation of a series of shock and expansion fans over the window. Density gradients associated with these shocks and expansion fans will create additional aero-optical distortions. Finally, if the relative velocity difference along the coolant gas interface is larger than the local speed of sound, traveling shocks and expansion fans will be created at the interface, causing additional optical distortions.

The modelling is critical for both predicting and mitigating aero-optical distortions. A physics-based weakly-compressible model for the aero-optical effects of a subsonic two-dimensional shear layer was developed by Fitzgerald and Jumper.[6,8] Assuming that the total temperature is the same on both sides of the shear layer, the model predicts that,

$$OPD_{rms} \sim K_{GD}\rho_\infty M_c^2 \Lambda, \tag{3}$$

where Λ is a characteristic shear layer length scale along the beam propagation direction. The convective Mach
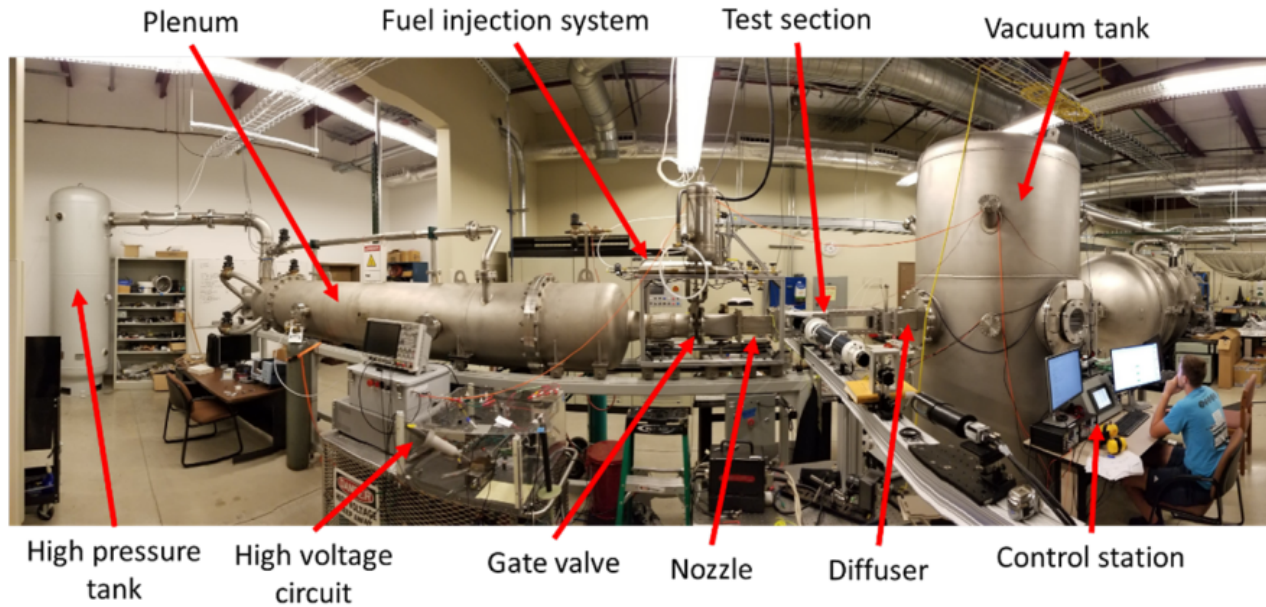
Figure 2: View of SBR-50 facility with components labeled.[11]

number, M_C, is defined as[9]

$$M_C = \frac{U_1 - U_2}{a_1 + a_2},\tag{4}$$

where U_1, a_1, and U_2, a_2 are the velocities and the speeds of sound, defined on the high- and the low-speed sides of the shear layer, respectively. It demonstrated that the model correctly predicts experimentally-observed levels of aero-optical distortions of subsonic and transonic shear layers.[6, 10]

Unfortunately, this model does not take into account a mixing of two different gases. Also, the total temperature of both mixing streams is assumed to be constant, which is not the case for the cooling mixing flows. Finally, the model works for subsonic and transonic speeds only. So, there is a need to extend this model to supersonic and hypersonic speeds for general temperature/species mismatched two-dimensional mixing layers.

In order to quantify aero-optical effects caused by two-dimensional cooling mixing flows over the window at high supersonic and hypersonic speeds, this paper presents preliminary results from a series of experiments over a generic but relevant flat cooled window inside a shallow cavity with a large length/depth ratio for a freestream Mach number of $M = 2$ for different mixing parameters, including total temperature ratios $T_{0,\infty}/T_{0,cool}$, and velocity ratios U_∞/U_{cool}, see Fig. 1(b).

3. EXPERIMENTAL SETUP

All experiments were performed in Notre Dame's SBR-50 tunnel in White Field Laboratories, which may be described as being configured as a combination of blowdown and Ludwieg tube schemes. The tunnel is designed for either $M = 2$ or $M = 4$ flow. For these experiments, $M = 2$ flow was selected. The driver section can be pressurized to stagnation pressures between 1 and 4 bar. A stagnation pressure of $P_0 = 2.6\ bar = 2.6 \times 10^5\ Pa$ was selected for all experiments. The driver section can also be heated to stagnation temperatures between 300K and 775K. Typical steady-state flow duration is 0.5-2 s.[11] An overview of the SBR-50 facility can be found in Fig. 2.

The test section insert, schematically shown in Fig. 3, is comprised of a larger aluminum frame, a 3-D printed plastic nozzle, and an aluminum cover plate with a thickness of 1 mm. These parts are secured to one another with screws. On the far upstream and far downstream edges, the test section insert conforms to the rest of the test section. In the center, the section is recessed. In addition, the test section insert contains an optical window
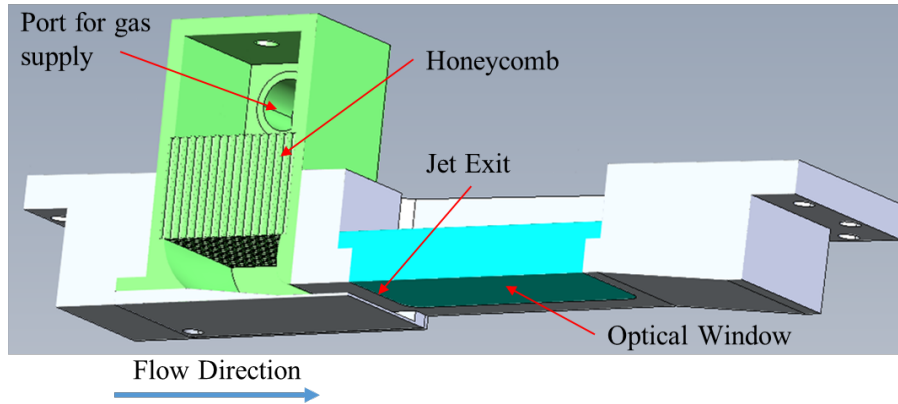
Figure 3: Diagram of a test section insert with a vertical cross-cut with components and features labeled.
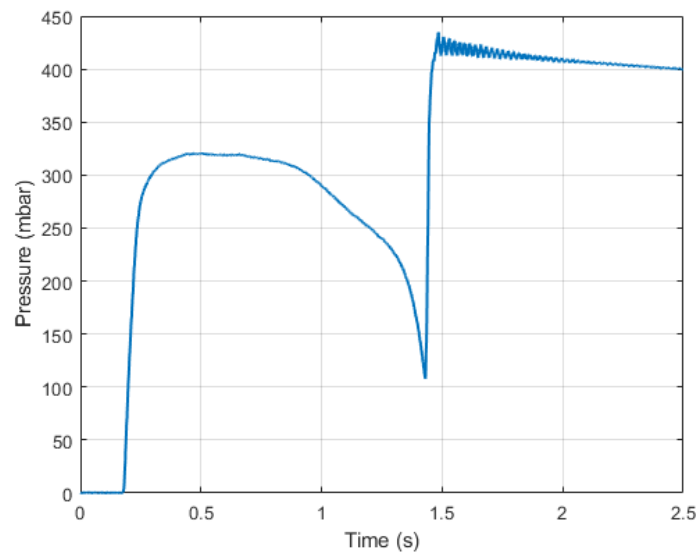

Figure 4: Time-dependent static pressure values from a pressure probe set downstream of the test section.

set downstream of the nozzle exit. The depth of the step is 5 mm and the span of the insert is 76 mm, the same as the test section span. Just upstream of the step, the height of the test section is approximately 77 mm. The optical window is set directly downstream of the exit of the nozzle, and has a length of 100 mm and a width of 50 mm. The overall length of the cavity is 108 mm. The nozzle exit has a cross-sectional area of approximately 289 mm^2. Both spanwise faces of the nozzle contain 1/2 NPT threaded holes for gas supply from a compressed air tank. In all experiments, the gas supply comprised of air pressurized to 9 $psig$ in order to match the static pressure between the exit jet in the freestream. In the midsection of the nozzle, a "honeycomb" mesh pattern is set in order to reduce turbulence from the gas supply. The nozzle section area is at a minimum at its exit, and therefore is designed to have an exit Mach number of 1. The upper face of the nozzle contains a 1/8 NPT threaded hole for a pressure probe to monitor the pressure of the gas supply.

For all tests, the gas supply was opened 500 ms after the tunnel flow startup and closed 1000 ms after the tunnel flow startup. This is because after 500 ms, the tunnel flow is fully developed and tunnel conditions become mostly steady until approximately 1 s, as shown by the pressure trace in Fig. 4.

Stagnation temperature in the wind tunnel was first kept at ambient condition of 295K, then heated between 350K and 750K in steps of 100K. A matrix of the test conditions can be found in Table 1.

A schematic of the optical measurements is presented in Fig. 5. As mentioned before, a large transparent flat

Table 1: Test conditions.

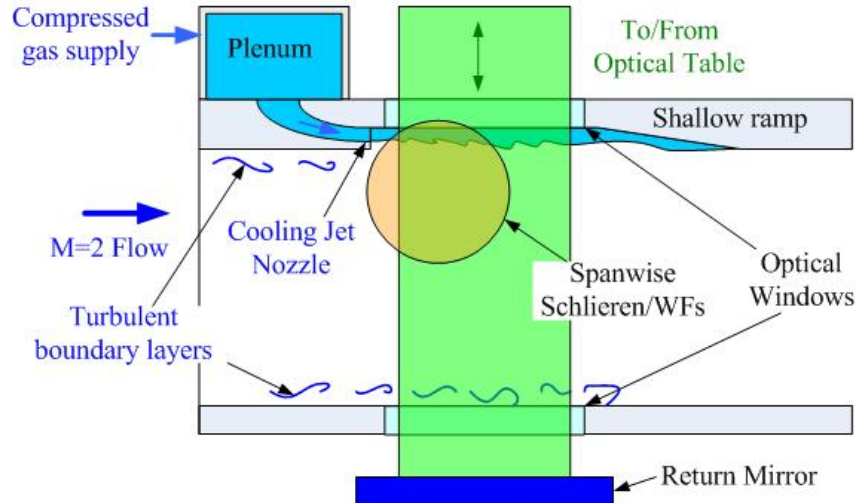| Run #	1	2	3	4	5	6
T_0	295 K	350 K	450 K	550 K	650 K	750 K
u_∞	510 m/s	560 m/s	630 m/s	700 m/s	760 m/s	820 m/s

Figure 5: Schematic of optical measurements.

optical window was flush-mounted into the floor of the cavity immediately downstream of the cooling jet nozzle. Another optical window of the same size was installed on the opposite (bottom) side of the tunnel test section to provide optical access in the wall-normal direction. A collimated laser beam 50 mm in diameter was forwarded into the test section in the wall-normal direction. After being reflected from a flat return mirror outside of the test section, the beam was sent back to the optical table exactly along the same path it came into, thus doubling the optical signal. The outgoing beam was forwarded into a high-speed Shack-Hartmann wavefront sensor (WFS) to measure time-resolved spatial wavefronts caused by the turbulent flow in the cavity. The high-speed camera used in all tests was a Phantom v2512 camera. The lenslet array placed on the camera lens has a pitch of 0.3 mm and a focal length of 38.2 mm. Tests were performed at a range of sampling frequencies between 75 kHz and 1 MHz. From this data, both deflection angles and wavefront data were obtained. A labelled picture of the Shack-Hartmann Wavefront Sensor setup is shown in Fig. 6.

To compliment the wall-normal optical measurements, a time-resolved Schlieren system in the spanwise-direction was used to qualitatively evaluate the flow topology of the incoming boundary layer and the mixing layer. Schlieren imaging was performed in the spanwise direction in order to qualitatively characterize the flow and to determine convective velocities via optical methods. The Schlieren setup consisted of an LED light source, two 5-inch diameter telescopes, and a vertical knife edge. A picture of the Schlieren setup is shown in Fig. 7.

The spatial resolution of the Schlieren setup was 8,800 pixels/m. A representative frame of the Schlieren image with the cooling nozzle flow on is shown in Fig. 8. An incoming turbulent boundary, a boundary layer on the opposite wall, and the resulting mixing layer over the cavity can be clearly seen. A weak oblique shock is also formed at the corner of the step.

4. DATA REDUCTION APPROACHES

4.1 Optical Velocity

In order to temporally resolve the moving structures at speeds close to freestream speed, the Schlieren image size was reduced to a resolution of 768x256 pixels, as shown in Fig. 9, enabling a higher recording rate of 100 kHz. Several areas of interest in the Schlieren images were identified, as shown in Fig. 9. Box A, with a size of 70x100 pixels, is located in the incoming boundary layer. Box B, with a size of 30x100 pixels, was placed at the
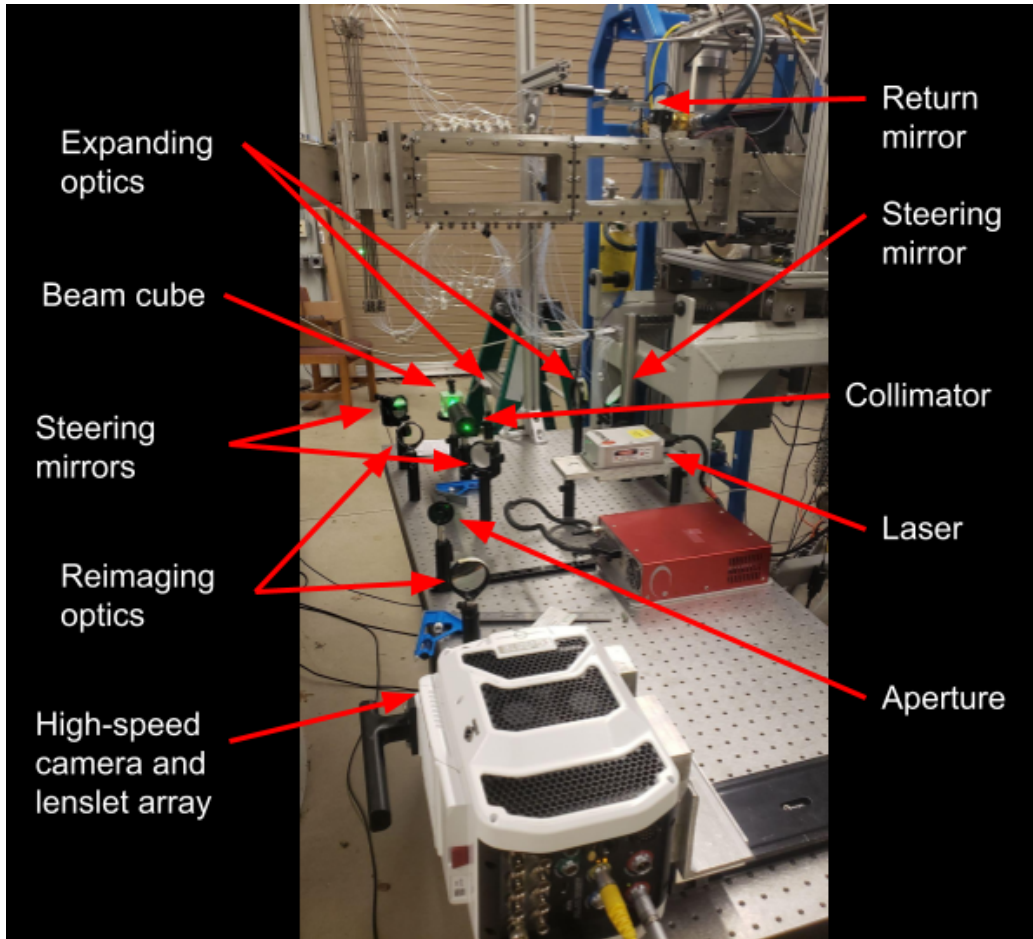
Figure 6: View of Shack-Hartmann WFS with components labeled.
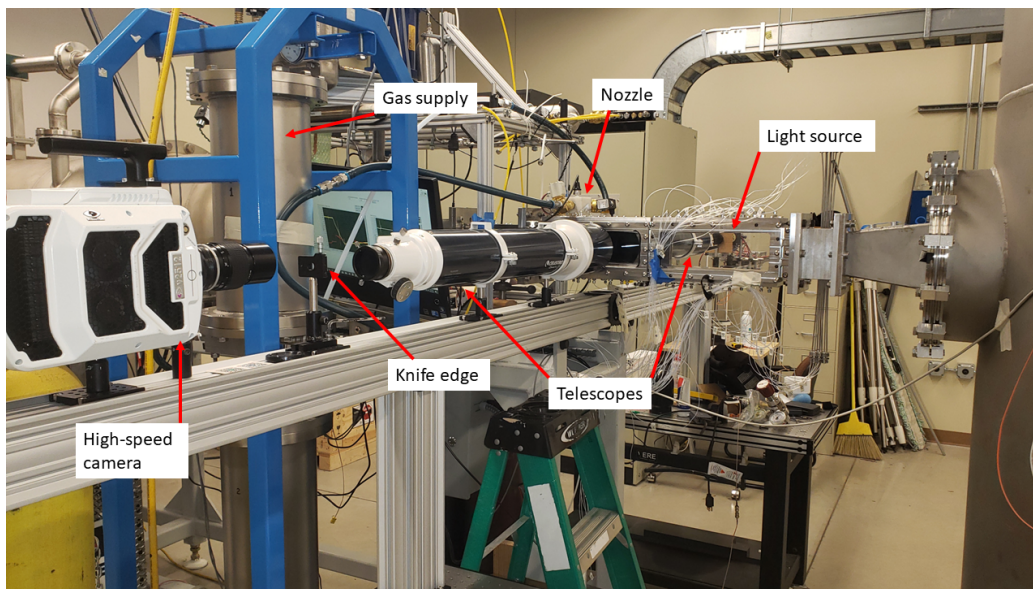

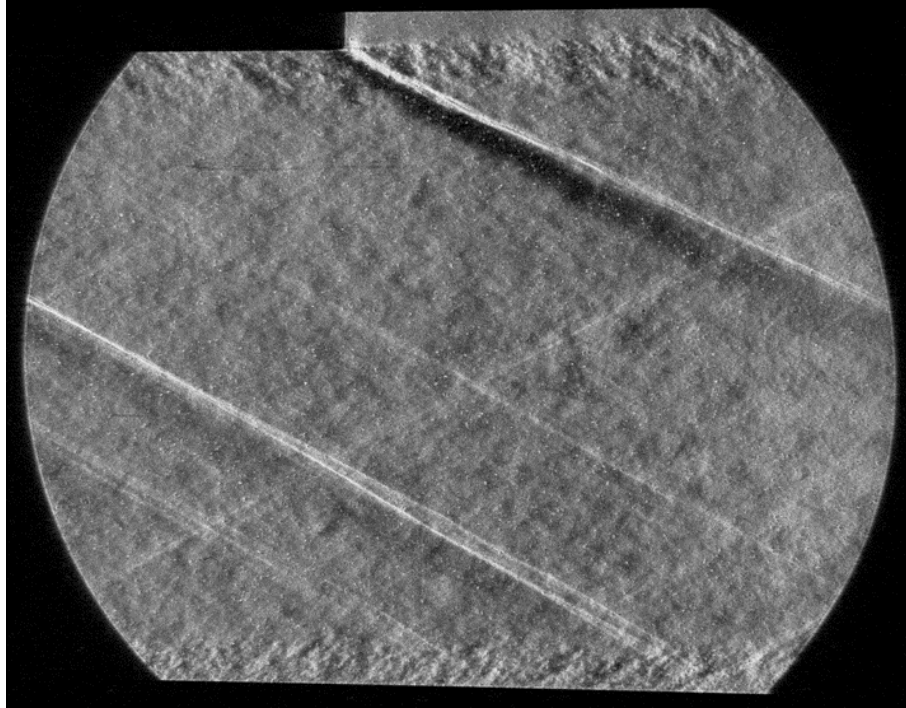Figure 7: View of Schlieren setup with components labeled.

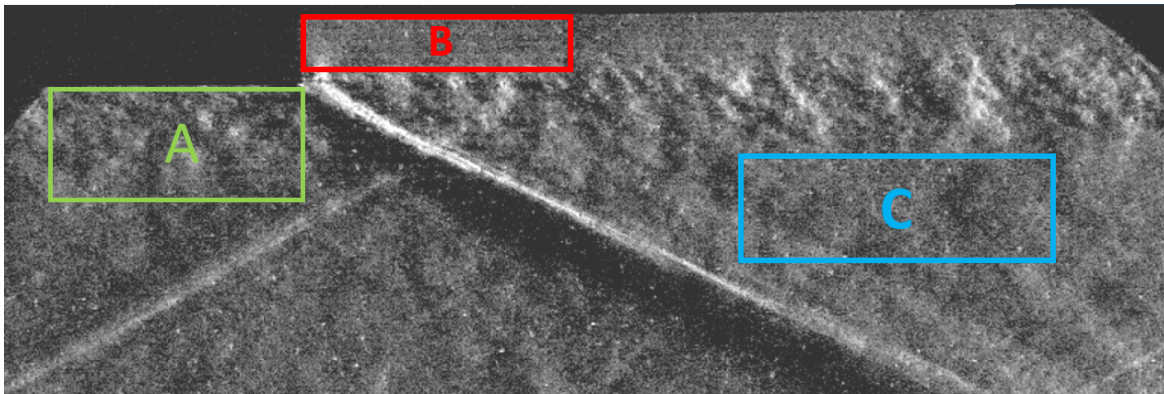Figure 8: Spanwise Schlieren image with nozzle flow on.

Figure 9: Schlieren image with areas of interest highlighted in color boxes.

exit of the cooling jet. Box C, with a size of 50x150 pixels, was positioned in the freestream flow region outside of the mixing layer.

Using the data from each identified box, spatio-temporal Fourier transform was performed on the mean-removed Schlieren image data at each wall-normal location. The number of spatial points used was dependent on the width of the area of interest. To reduce computing time, only the first 10,000 temporal points (with a total duration of 0.1 sec) after the nozzle flow was turned on were used. No windowing or block averaging was used in the analysis. The Fourier power spectrum, taken from the Schlieren data inside Box C, is shown in Fig 9. The convective nature of the aero-optical distortions is manifested as a diagonal branch, identified by solid circles. The slope of this branch, obtained by performing a linear fit (indicated by a dashed line), is equal to the inverse of the convective speed, U_c, of these convecting structures at this wall-normal location.

In addition to the main branch, many other branches are present in Fig. 10(a) above and below the main branch due to aliasing of the main branch in the frequency domain. To extend the frequency range in the main branch and to improve the accuracy of the convective velocity estimate, a stacking method[12, 13] was used. In the stacking method, copies of the 2-D spectrum, shifted by a multiple of the sampling frequency in both

positive and negative frequency directions, are added to the original spectrum to reduce aliasing. The resulting extended spectrum is shown in Fig. 10(b). Note that the original 2-D spectrum has been stacked once on either side in the temporal frequency space. The resulting spectrum shows a well-defined "branch" in both spatial and temporal frequency, with more points in the frequency range. The extended convective branch is identified by computing local weighed maxima, indicated by solid red circles. For every extended spectrum at a given wall-normal location, the linear fit was used to calculate the convective speed at this location.
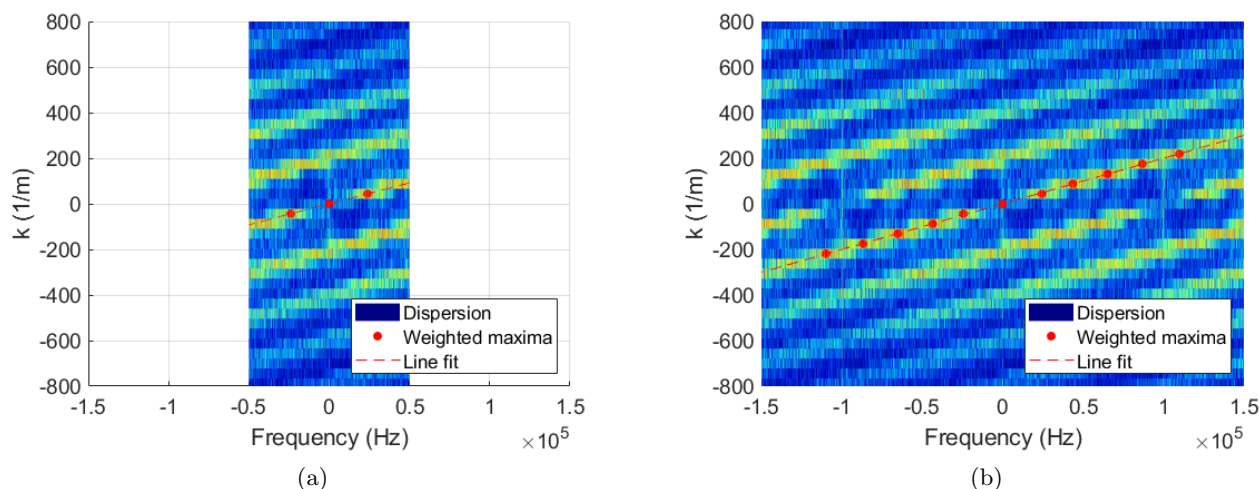

Figure 10: 2-D Fourier transforms of a horizontal section of Schlieren data with convective velocity line fit overlaid, (a) without stacking (b) with stacking.

4.2 Aero-optical distortion levels

The Shack-Hartmann sensor measured deflection angles (θ_x, θ_z) at discrete locations (x, z) over the aperture. The deflection angles are related to the wavefront, $OPD(x, z, t)$, via the spatial gradient, $\theta_x = \partial OPD/\partial x, \theta_z = \partial OPD/\partial z$. In-house software was used to numerically integrate the measured deflection angles to obtain the wavefront time sequences over the aperture using Southwell's method.[14] To make the solution unique, the spatial mean value of the wavefront (piston component) was forced to zero at every time, $\int OPD(x, z, t)dxdz = 0$. In addition, the time-averaged wavefront (steady lensing) and instantaneous tip/tilt component were removed from each wavefront. Finally, the aperture-averaged levels of aero-optical distortion, OPD_{rms}, were calculated using Eq. 2 for different test conditions.

5. RESULTS

5.1 Speed and Temperature Estimates from Schlieren Data

From the analysis of convective velocities for Schlieren data, velocity profiles at the nozzle exit, the upstream boundary layer, and multiple downstream locations within the mixing layer were computed, as described before. The convective velocity profiles, extracted in the region of the incoming boundary layer, indicated as box A in Fig. 9, are presented in Fig. 11. The velocities are normalized by the estimated freestream velocity required for all boundary layer profiles to approximately collapse on top of one another, at least in the boundary layer region. The normalized velocity profiles monotonically increase father away from the wall, as expected for the boundary layer. The boundary layer thickness can be estimated as approximately 5 - 6 mm. Note that the velocity ratio at the edge of the boundary layer is not 1, but close to 0.93. Similar velocity ratios were observed in other optical spanwise measurements for the boundary layers, and attributed to the additional optical distortions due to boundary layers present along side walls.[12] Also note that data points become more scattered further from the wall. This is likely attributable to a lack of discernible convective turbulent structures in the freestream region.
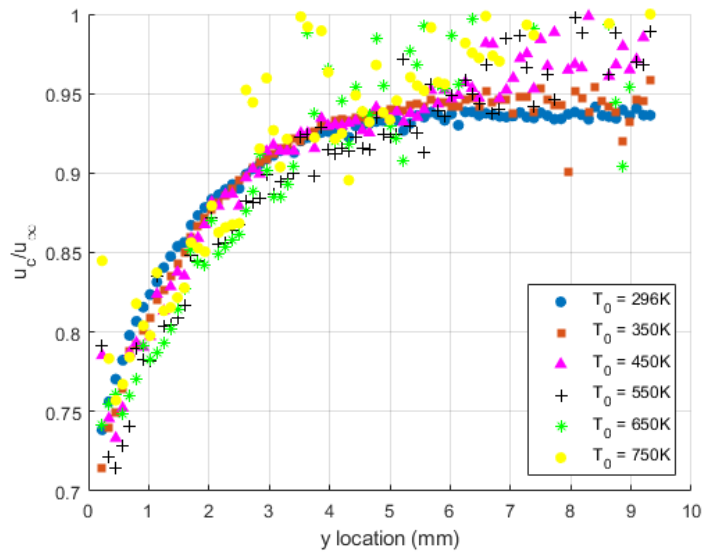
Figure 11: Extracted convective velocity profiles for the incoming boundary layer using freestream total temperatures.
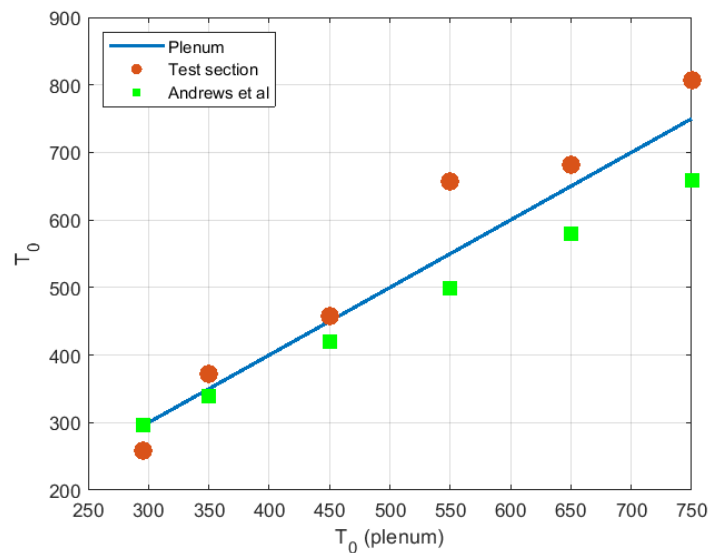

Figure 12: Estimated total temperatures in the test section, using the convective speeds, as a function of plenum total temperatures. Estimates of the total temperatures in the test section from Andrews et. al.[11] are also shown.

From the wall-normal averaged freestream velocities, computed from box C, the estimation of the total temperatures in the test section was performed, assuming adiabatic flow. Results for different plenum total temperatures are presented in Fig. 12 as red circles. The total freestream temperatures, denoted by green squares, calculated in a different flow characterization study of the SBR-50 tunnel[11] are also presented in Fig. 12. Total temperatures estimated from the optical data agree reasonably well with the total temperature from,[11] although consistently higher in value.

The nozzle exit velocities, extracted from the region indicated by box B in Fig. 9 and averaged over all wall-normal locations, are shown in Fig. 13. It can be seen that the nozzle exit velocity is consistent across varied freestream total temperatures, as expected.
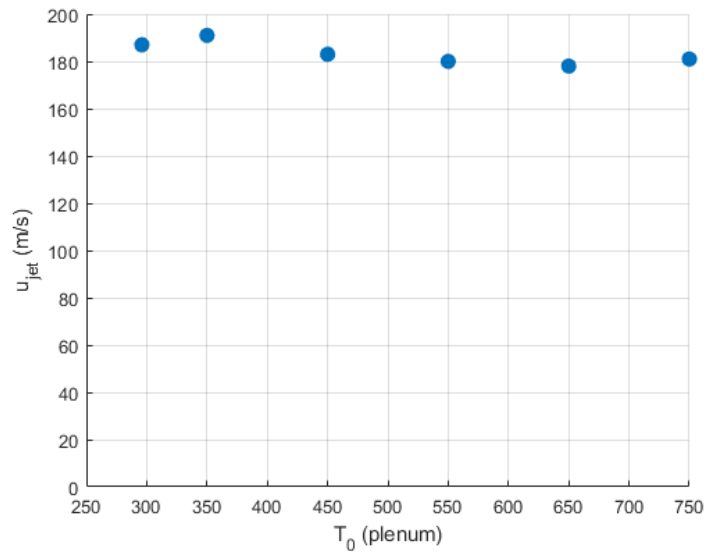
Figure 13: Estimated nozzle exit velocities as a function of freestream total temperatures

5.2 Mixing Layer Thickness

In order to quantify the thickness of the mixing layer at different downstream locations from the Schlieren data, the temporal standard deviation of the intensity values at each pixel was calculated. An example of this is shown in Fig. 14. High intensity variation can be observed at the oblique shock originating from the edge of the step, the incoming boundary layer, and the mixing layer. Intensity variations at selected downstream locations, measured from the beginning of the mixing flow, are shown in Fig. 15. It can be seen that intensity variation is biased toward higher wall-normal locations, due to the presence of the oncoming boundary layer. To account for this, only the half of the peak closer to the wall was taken, then mirrored. After mirroring, the curve then becomes symmetric, and a Gaussian curve can be fitted to the intensity values, and the half-width of the curve calculated. This provides a metric for the local mixing layer thickness, δ_{ML}, the results of which for different total temperatures are shown in Fig. 16. The thickness increases approximately in a linear fashion in the streamwise direction, as expected for mixing layers. The mixing layer becomes thinner at higher freestream temperatures above 500K. The reasons of why the mixing layer is abnormally thicker for 450K are not clear at this point and require further investigation.

5.3 Levels of Aero-Optical Distortions and Proposed Model

The collected wavefronts were processed, as discussed before, and the overall levels of aero-optical distortions by the mixing layer were computed using Eq. 2 for different freestream total temperatures. The obtained experimental results for different total temperatures versus the subsonic model, Eq. 3, are presented in Fig. 17(a); clearly the model does not work at supersonic speeds. This is expected, as it was mentioned in the Introduction, that the existing model fails to work at supersonic speeds. Still, the the model correctly identified the main source of aero-optical distortions in the subsonic and transonic shear layers, which are regions of lower pressure, referred to as pressure "wells", inside the large-scale coherent vortical structures rotating flow in the streamwise/wall-normal plane.[8] The pressure gradient of these "wells" balances the centripetal acceleration of the rotating flow. It is straightforward to derive[6] that the pressure drop, ΔP, inside the vortical structure is

$$\Delta P \sim \rho_{ref}(U_\infty - U_c)^2, \tag{5}$$

where ρ_{ref} is some reference density and U_c is the convective speed of the mixing layer, which can be estimated as[9]

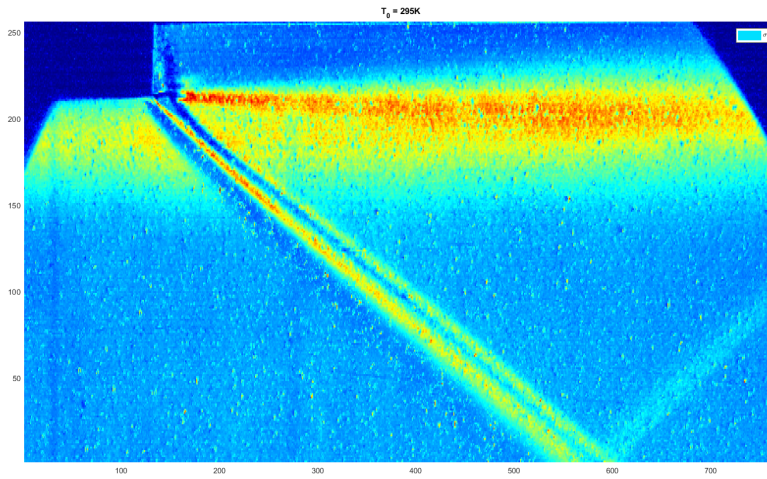$$U_c = \frac{a_{cool}U_\infty + a_\infty U_{cool}}{a_\infty + a_{cool}}. \tag{6}$$

Figure 14: Temporal standard deviation of intensity, $T_0 = 295K$. Pixel numbers are plotted on axes.
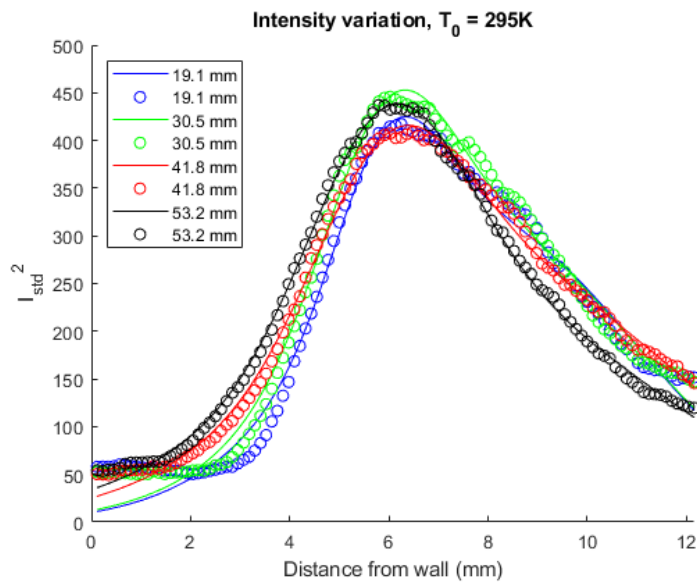

Figure 15: Temporal standard deviation of intensity at various downstream locations, $T_0 = 295K$.
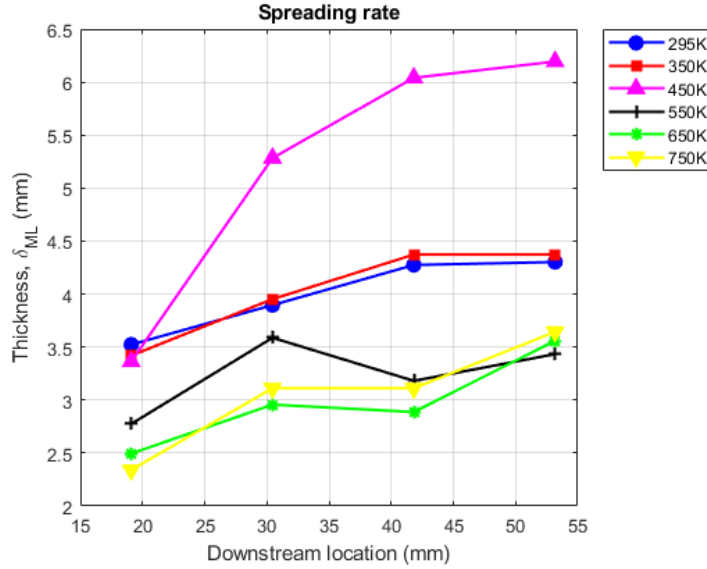
Figure 16: Streamwise evolution of the mixing layer thicknesses, based on half-width of intensity variations, at different total temperatures.

Here and below the sub-index "cool" represents the conditions at the cooling side of the mixing layer. Assuming an isentropic flow and small density/pressure variations, using the equation of state and the definition of Mach number, the density drop inside the vortical structure becomes

$$\frac{\Delta P}{P_\infty} = \gamma \frac{\Delta \rho}{\rho_{ref}} \sim \gamma \frac{\rho_{ref}(U_\infty - U_c)^2}{P_\infty} \sim \left(\frac{U_\infty - U_c}{a_{ref}}\right)^2. \tag{7}$$

Finally, using the definition of OPD from Eq. 1 and assuming that the OPD_{rms} is proportional to OPD, we can get a new scaling for the aero-optical distortions of the supersonic shear layers,

$$OPD_{rms} \sim K_{GD}\Delta\rho\Lambda \sim K_{GD}\Lambda\rho_{ref}\left(\frac{U_\infty - U_c}{a_{ref}}\right)^2, \tag{8}$$

where Λ is a characteristic thickness of the mixing layer along the beam propagation. In these studies a half-width of the mixing layer at the downstream location of 42 mm from Figure 16 were used, $\Lambda = \delta_{ML}$. It is straightforward to show that in the limit of subsonic speeds and total-temperature-matched flows, Eq. 8 becomes Eq. 3.[6] Also note that the model does not explicitly specify the choice of the reference values.

When the experimentally-measured values of OPD_{rms} are plotted against the new proposed model, Eq. 8, as open circles, the agreement, while still showing some scatter, is better, see Fig. 17(b). In this comparison, we chosen $a_{ref} = a_{cool}$ and $\rho_{ref} = \rho_\infty$. In reality, both the reference speed of sound and the reference density might be some combination of the freestream and the cooling jet properties, potentially improving the model agreement with the experimental data.

From Fig. 8 it can be seen that the aero-optical distortions measured in the wall-normal direction will include not only the mixing layer, but also contaminating aero-optical distortions from the boundary layer on the opposite (bottom) wall and the oblique shocks in the middle of the test section. Assuming that the boundary layer on the opposite wall has the same thickness of 5 mm as the incoming boundary layer, it is possible to estimate and remove contaminating aero-optical effects of the boundary layer, using the model and experimental measurements presented in Refs. 13, 15. The resulted OPD_{rms} are shown in Fig. 17(b) as red stars; the agreement with the model, indicated as a dashed line, is even better. Removing the additional contaminating effects of the oblique shocks in the freestream region is expected to further improve the agreement with the proposed model.
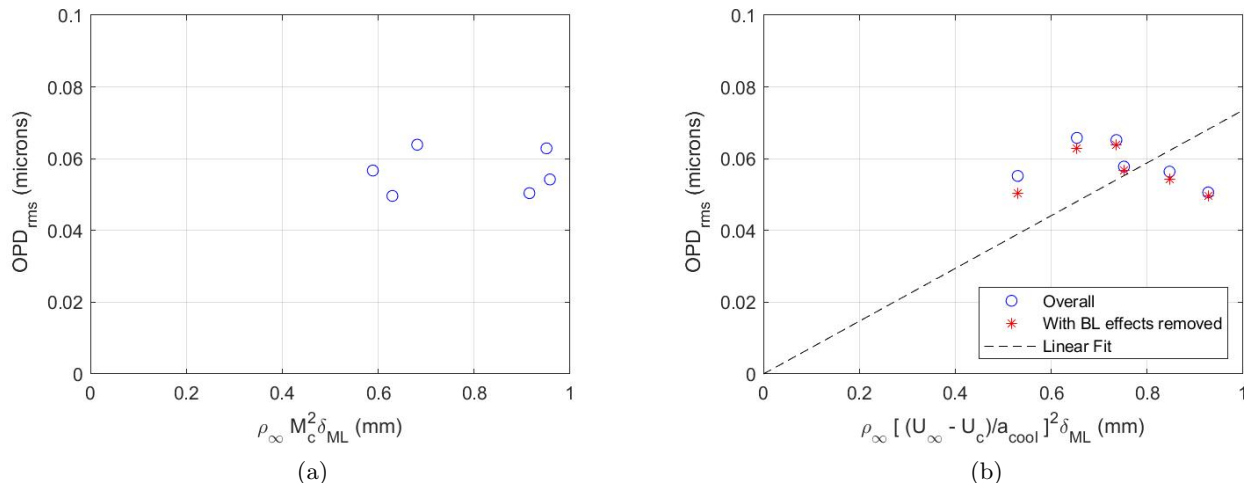
Figure 17: (a) OPD_{rms} versus subsonic scaling $\rho_\infty M_c^2$, Eq. 3. (b) OPD_{rms}, without and with contaminating effects of the opposite boundary layer removed, versus a new proposed scaling $\rho_\infty[(U_\infty - U_c)/a_{cool}]^2$, Eq. 8.

6. CONCLUSIONS

Optical measurements of a temperature-mismatched supersonic mixing layer were made using time-resolved Shack-Hartmann WFS and Schlieren photography measurement techniques. The mixing layer was created by a $M \approx 0.56$ jet blown through a backward-facing step with a depth of $5mm$. The jet was placed at the wall of a $M = 2$ wind tunnel and connected to an external gas supply pressurized to $9psig$ to match the static pressure in the test section. Spanwise Schlieren measurements in the spanwise direction over an area with a diameter of $125\ mm$ were made at sampling frequencies of 25 kHz and 100 kHz. Wall-normal Shack-Hartmann WFS measurements in the direction normal to the mixing layer with a beam diameter of $50\ mm$ were performed just downstream of the cooling nozzle exit. Wind tunnel total temperature was varied between $T_0 = 295K$ and $T_0 = 750K$.

Flow parameters including boundary layer thickness, freestream and jet velocity, and shear layer thickness were extracted from Schlieren measurements using optical velocity techniques. OPD_{rms} values were extracted from Shack-Hartmann WFS data. A new scaling model was proposed, based on optical distortions induced by pressure "wells" inside the coherent vortical structures in the streamwise/wall-normal plane. The proposed model provides a better agreement to the experimental data than the previous subsonic model. The model can be used to predict aero-optical distortions caused by cooling flow over optical windows on supersonic or hypersonic vehicles.

These experiments do not address species-mismatched mixing layers. Future experiments will use other cooling gases such as He and CO_2 to examine this highly relevant parameter.

Acknowledgements

REFERENCES

[1] Juhany, K. A., Hunt, M. L., and Sivo, J. M., "Influence of injectant mach number and temperature on supersonic film cooling," *Journal of Thermophysics and Heat Transfer* **8**(1), 59–67 (1994).

[2] Aupoix, B., Mignosi, A., Viala, S., Bouvier, F., and Gaillard, R., "Experimental and numerical study of supersonic film cooling," *AIAA Journal* **36**(6), 915–923 (1998).

[3] Sahoo, N., Kulkarni, V., Saravanan, S., Jagadeesh, G., and Reddy, K. P. J., "Film cooling effectiveness on a large angle blunt cone flying at hypersonic speed," *Physics of Fluids* **17** (02 2005). 036102.

[4] Zhang, W., Ju, L., Fan, Z., Fan, W., and Chen, S., "Optical performance evaluation of an infrared system of a hypersonic vehicle in an aero-thermal environment," *Opt. Express* **31**, 26517–26534 (Jul 2023).

[5] Wang, M., Mani, A., and Gordeyev, S., "Physics and computation of aero-optics," *Annual Review of Fluid Mechanics* **44**(1), 299–321 (2012).

[6] Gordeyev, S., Jumper, E., and Whiteley, M., [*Aero-Optical Effects: Physics, Analysis and Mitigation*], Wiley Series in Pure and Applied Optics, Wiley (2023).

[7] Kalensky, M., Wells, J., and Gordeyev, S. V., "Image degradation due to different in-flight aero-optical environments," *Optical Engineering* **59**(10), 104104 (2020).

[8] Fitzgerald, E. J. and Jumper, E. J., "The optical distortion mechanism in a nearly incompressible free shear layer," *Journal of Fluid Mechanics* **512**, 153–189 (2004).

[9] Papamoschou, D. and Roshko, A., "The compressible turbulent shear layer: an experimental study," *Journal of Fluid Mechanics* **197**, 453 – 477 (1988).

[10] Kemnetz, M. R., "Analysis of the aero-optical component of the jitter using the stitching method," (2019).

[11] Andrews, P., Lax, P., Elliott, S., Firsov, A., and Leonov, S., "Flow characterization at heated air supersonic facility sbr-50," *Fluids* **7**(5) (2022).

[12] Sontag, J. and Gordeyev, S., "Optical diagnostics of spanwise-uniform flows," *AIAA Journal* **60**(9), 5031–5045 (2022).

[13] Lynch, K. P., Miller, N. E., Guildenbecher, D. R., Butler, L., and Gordeyev, S., "Aero-Optical Measurements of a Mach 8 Boundary Layer," *AIAA Journal* , 1–11 (2022).

[14] Southwell, W. H., "Wave-front estimation from wave-front slope measurements," *Journal of the Optical Society of America (1917-1983)* **7**, 998 (Aug. 1980).

[15] Gordeyev, S., Smith, A. E., Cress, J. A., and Jumper, E. J., "Experimental studies of aero-optical properties of subsonic turbulent boundary layers," *Journal of Fluid Mechanics* **740**, 214â€"253 (2014).